Role of optical anisotropies in the polarization properties of surface-emitting semiconductor lasers

M. Travagnin,*,† M. P. van Exter, A. K. Jansen van Doorn, and J. P. Woerdman
Huygens Laboratorium, Leiden University, P.O. Box 9504, 2300 RA Leiden, Netherlands
(Received 20 December 1995)

Due to the transverse device symmetry, the polarization properties of the light generated by surface-emitting semiconductor lasers will be strongly influenced by residual anisotropies. We describe the polarization dynamics of these lasers on the basis of a theoretical model founded on the coexistence of two different electron-hole recombination transitions, which give rise to circularly polarized fields with opposite helicities; the carrier densities available for these two transitions are coupled via spin-mixing processes. The residual cavity anisotropies are introduced in the model by means of the boundary conditions imposed to the counterpropagating fields: anisotropies which are symmetric and antisymmetric under time reversal will generate different boundary conditions. We include in the equations the effects of material strain, which causes symmetric linear phase and amplitude anisotropies, and of an externally applied magnetic field, which induces antisymmetric circular phase and amplitude anisotropies via the Faraday effect. This theoretical framework allows us to explain, with realistic values of the system parameters, some of the polarization behaviors exhibited by surface-emitting semiconductor lasers, namely, bistability and switching between orthogonal linearly polarized fields and magnetically induced ellipticity. [S1050-2947(96)01908-7]

PACS number(s): 42.55.−f

I. INTRODUCTION

A vertical cavity surface-emitting laser (VCSEL) is characterized, as compared with conventional edge-emitting semiconductor lasers, by an active layer *orthogonal* to the cavity axis and by light emission *parallel* to the device growth direction [1,2]. From the nominal transverse symmetry which follows from this geometry stems one of the most distinctive advantage of VCSEL's, that is, the absence of astigmatism in the emitted light.

On the other hand, while the light generated by edge-emitting lasers is always linearly polarized along one of the transverse axes defined by the laser stripe, such simplicity is not to be expected in VCSEL's: in the absence of any designed transverse asymmetry, their polarization properties will be in fact strongly influenced by the residual anisotropies of the material, and in particular by the linear anisotropies due to unintentional strain.

In effect, an increasing number of experiments shows that the light generated by VCSEL's may exhibit a rich variety of polarization behaviors. The fundamental transverse mode is usually found to be linearly polarized [3], but the polarization direction changes with increasing pumping current [4]; higher-order transverse modes are also found to be linearly polarized, but their polarization direction is orthogonal to the polarization direction of the fundamental mode [5]. Bistability and switching among linearly polarized states with orthogonal polarization directions have also been reported [6].

A common explanation for the switching between linearly polarized states of emission relies on the variations induced by temperature changes in the gain spectral profile and in the eigenfrequencies of the linearly polarized states, which are split by the linear phase anisotropy [7]. This gain-differential theory does not seem to suit VCSEL's very well, due to the smallness of the frequency splitting as compared to the large spectral width of the gain profile.

Only lately has a theoretical investigation specifically intended for VCSEL's been started by San Miguel, Feng, and Moloney (SFM) [8]. These authors develop a model which, neglecting for simplicity all Coulomb interactions and energy dispersions, takes into account two distinct carrier populations characterized by opposite spin and includes their influence on the field phase, via the linewidth enhancement factor [9]. When a linear phase anisotropy is added, the SFM model effectively gives as stationary solutions linearly polarized states oriented along two preferred orthogonal directions and discriminated in their stability properties by transverse effects, i.e., by diffraction [8]. In a very recent paper it has been demonstrated that the SFM approach can also lead to rich nonlinear dynamics and that polarization switching can take place if an external signal is injected in the laser [10].

The motivation of the present paper is rooted in the recent experimental demonstration that the application of an axial magnetic field significantly modifies the polarization characteristics of VCSEL's [11]. From the theoretical point of view, this demonstration sets the necessity of an integrated analysis of the role of linear and circular anisotropies on the polarization properties of VCSEL's, since generally the linear anisotropies cannot be avoided. The aim of the present paper is precisely to present such an analysis, on the basis of the original SFM framework.

As soon as the influences of a circular anisotropy are to be investigated, it becomes necessary to distinguish the effects of a magnetic field from the effects of a possible optical activity in the laser material. Luckily, although both Faraday effect and optical activity give rise to circular phase anisotro-

*Electronic address: Trava@rulhm1.leidenuniv.nl
†Permanent address: Dipartimento di Fisica, Università di Milano, Italy. Electronic address: Travagnin@mi.infn.it

pies, they can be discriminated on the basis of their behavior under time reversal, or, equivalently, on the basis of their action on the fields which are counterpropagating inside the laser cavity. We will therefore begin our theoretical investigation one step before what was done in [8], starting from the equation of counterpropagating fields and applying the boundary conditions due to the various cavity anisotropies according to the formalism described in [12,13]; only in this way can it be demonstrated that optical activity has no net effects in a mean-field limit, and consequently that the sole origin of circular phase anisotropies is the magnetic field. By setting the magnetic field to zero we recover some of the results reported in [10].

The material of the paper is organized as follows: after this general introduction, we present in Sec. II the quantum scheme of the laser and include the influence of optical anisotropies, both linear and circular, in the system dynamics, to derive finally the fundamental equations which regulate the polarization properties of VCSEL's. In Sec. III we examine the role of the linear anisotropies which follow from material strain, first determining the system stationary states and secondly analyzing their stability characteristics. In Sec. IV we study the influence of the circular anisotropies which follow from the application of an axial magnetic field, determining first the stable states of the system and then finding their analytical expressions close to the lasing threshold. Finally, in Sec. V, we summarize the results and present some possibilities for future work.

II. THEORETICAL FRAMEWORK

As in every laser, the polarization properties of the light generated by VCSEL's depend both on the quantum numbers of the angular momentum in the states between which the optical transitions takes place and on the transverse design of the laser cavity. The aim of the present section is to derive a set of equations which relate the polarization behavior of VCSEL's to the quantum structure of the active medium and to the anisotropies of the cavity.

The first anisotropy to deal with is the unavoidable linear phase anisotropy due to the strain induced into the material by lattice mismatch or by electrical contacts. As a consequence of this anisotropy, the orientation degeneracy of the electric field in the transverse plane will be removed and the frequencies of orthogonally linearly polarized light fields will be split.

A recent experiment [11] has shown that the application of an axial magnetic field to a VCSEL alters appreciably the polarization properties of the laser beam and that important physical parameters can be deduced by comparing this effect with theoretical models. In order to provide such a model, we will include in the equations governing the laser dynamics the circular phase anisotropy induced via the Faraday effect, which splits the frequencies of circularly polarized light fields with opposite helicities.

The complex nature of the refractive index in dispersive media imposes, via the Kramers-Kronig relations, the presence of amplitude anisotropies as soon as phase anisotropies are admitted. We will therefore generalize the equations governing the light polarization dynamics in VCSEL's to include the effect of linear and circular amplitude anisotropies.

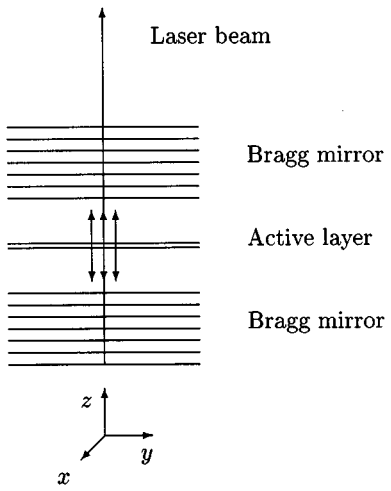

FIG. 1. Schematic representation of a vertical cavity surface-emitting laser.

A. Quantum scheme

The simplified representation of a VCSEL is shown in Fig. 1: two distributed Bragg reflectors separated by a spacer that contains the gain medium, which usually consists of one or more quantum wells. Light is coupled out through the top surface of the wafer. The cross section of the device is usually circular, so that the laser has an overall cylindrical symmetry. For the band structure of the active layer in a quantum well VCSEL we follow the SFM model [8], summarized in Fig. 2. If spin-orbit interaction is neglected, the relevant quantum numbers are, respectively, l and m_l for the orbital angular momentum and its z component, and m_s for the z component of the spin angular momentum. The conduction band is characterized by the values $l=0$, $m_l=0$, and $m_s=\pm 1/2$ and consequently has only spin degeneracy, while the valence band, characterized by $l=1$, $m_l=0,\pm 1$, and $m_s=\pm 1/2$, has both spin and angular momentum degeneracy. When spin-orbit interaction is taken into account the quantum numbers become j and m_j, respectively, for the total angular momentum and its z component. The conduction band is now identified by the values $j=1/2$ and $m_j=\pm 1/2$, while the valence band loses its angular momentum degeneracy, giving rise to four degenerate states $j=3/2$, $m_j=\pm 1/2,\pm 3/2$, which have a higher energy than the two degenerate states $j=1/2$, $m_j=\pm 1/2$. When the effect of quantum confinement along the z direction is added, the residual angular momentum orientation degeneracy of the $j=3/2$ state is also removed. The level $m_j=\pm 3/2$ is shifted upward and gives rise to the so-called heavy-hole band, while the level $m_j=\pm 1/2$ is shifted downward and gives rise to the light-hole band [14,15]. As in the SFM model, we will assume in the following that the splitting due to quantum confinement is large enough to rule out transitions between the conduction and the light-hole valence band, thus assuming that the active material of the vertical cavity surface-emitting laser can be described by the simplified four-level scheme shown in Fig. 2(b). Note that the selection rule $\Delta m_j=\pm 1$ allows two different transitions between the conduction and the heavy-hole valence band, both associated with the generation of circularly polarized light:

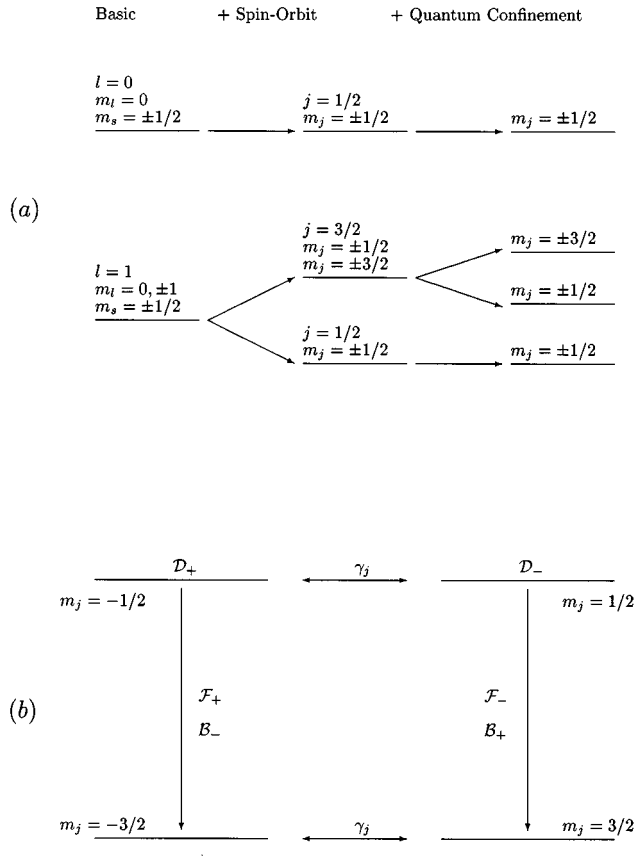

FIG. 2. (a) Band structure of a quantum well VCSEL. (b) Energy levels relevant for lasing transitions in VCSEL's: both the transitions shown are associated with circularly polarized light. The symbols $\mathcal{F}_+$, $\mathcal{F}_-$, $\mathcal{B}_+$, and $\mathcal{B}_-$ indicate the forward- and backward-propagating fields with opposite helicity. The carriers densities available for the two transitions—indicated by $\mathcal{D}_+$ and $\mathcal{D}_-$—are coupled to each other through spin–mixing processes characterized by an overall rate γ_j.

in the following we will indicate with $\mathcal{D}_\pm(z,t)$ the carrier inversion densities available for these two transitions.

The dimensionless slowly varying envelopes of the circularly polarized complex fields $\mathcal{F}_\pm(z,t)$ and $\mathcal{B}_\mp(z,t)$ which propagate respectively in the forward and backward directions have been sketched in Fig. 3. The subscripts indicate the helicity of the fields, that is, the projection of the photon intrinsic angular momentum on the direction of propagation [16]: accordingly, we have interchanged the subscript signs in the backward field with respect to the forward field. Since the same electronic transition generates counterpropagating fields with opposite helicity, the carrier density $\mathcal{D}_+$ available for the transition $m_j=-1/2\rightarrow-3/2$ will couple with $\mathcal{F}_+$ and $\mathcal{B}_-$, while the carrier density $\mathcal{D}_-$ available for the transition $m_j=1/2\rightarrow3/2$ will couple with $\mathcal{F}_-$ and $\mathcal{B}_+$ [see Fig. 2(b)].

Note that it has been assumed that all the system variables $\mathcal{D}_\pm$, $\mathcal{F}_\pm$, and $\mathcal{B}_\mp$ do not depend on the transverse coordinates x and y: this means that the diffusion of the carriers and the diffraction of the light have been neglected, and therefore all our analysis will be valid in the limit of the plane-wave approximation.

The time scale of the various processes involved in the dynamics of a VCSEL is described by the following rates.

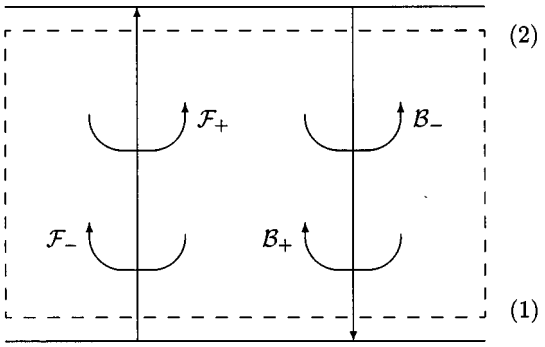

FIG. 3. Conventions used to indicate the circularly polarized fields $\mathcal{F}_\pm$ and $\mathcal{B}_\mp$ which counterpropagate inside the laser cavity; the active material has been represented with a dashed box, and the distributed Bragg reflectors have been replaced by two equivalent hard mirrors. Note that the helicity changes upon every reflection.

(i) the field cavity decay rate κ, equal to one half of the inverse photon lifetime, which is $\approx10^{12}$ s^{-1};

(ii) the inverse carrier radiative lifetime $\gamma_\parallel$, which is $\approx10^9$ s^{-1};

(iii) the spin-mixing rate γ_j, which is determined in a complicated way by a number of different scattering mechanisms [17,18] and in quantum wells is estimated to be in the range 10^{10}–10^{11} s^{-1};

(iv) the material polarization relaxation rate $\gamma_\perp$, which is in the range 10^{13}–10^{14} s^{-1}.

Due to the strong inequality $\gamma_\perp\gg\kappa,\gamma_j,\gamma_\parallel$, the material polarization can be adiabatically eliminated from the system of equations which governs the laser dynamics, and a rate-equations approach can be followed. The laser dynamics is therefore fully described by the fields $\mathcal{F}_\pm(z,t)$ and $\mathcal{B}_\mp(z,t)$ and by the carrier inversion densities $\mathcal{D}_\pm(z,t)$. With a proper choice of the reference frequency the counterpropagating fields obey the partial differential equations [19]

$$\frac{\partial\mathcal{F}_\pm}{\partial t}+v_0\frac{\partial\mathcal{F}_\pm}{\partial z}=g'(1-i\alpha)\mathcal{D}_\pm\mathcal{F}_\pm, \tag{1a}$$

$$\frac{\partial\mathcal{B}_\mp}{\partial t}-v_0\frac{\partial\mathcal{B}_\mp}{\partial z}=g'(1-i\alpha)\mathcal{D}_\pm\mathcal{B}_\mp, \tag{1b}$$

where v_0 is the velocity of light in the material, g' is the gain per unit inversion and unit time (with the dimension of a volume divided by time), and the linewidth enhancement factor α ($\alpha>0$) takes account of the influence of the carrier density on the material refractive index [9].

A considerable simplification of the problem can be achieved if the longitudinal variations of the system variables are so small that the laser can equally well be described by their z averages; in fact, the high reflectivity of the VCSEL Bragg mirrors guarantees the validity of this longitudinal quasiuniformity or mean-field assumption. In the following, we will treat the distributed reflectors as identical hard mirrors placed very close to the boundaries (1) and (2) of the active layer, choosing the zero of the vertical axes in such a way that these boundaries lie respectively in the planes $z=0$ and $z=L$, where L is the active layer length (see

Fig. 1 and Fig. 3). The effect of the reflection losses is included in the model by rescaling the variables according to the relations [19]

$$\tilde{\mathcal{F}}_{\pm}(z,t)=\exp\left[-\frac{1}{2}\left(\frac{z}{L}-1\right)|\ln R|\right]\mathcal{F}_{\pm}(z,t), \tag{2a}$$

$$\tilde{\mathcal{B}}_{\mp}(z,t)=\exp\left[\frac{1}{2}\left(\frac{z}{L}\right)|\ln R|\right]\mathcal{B}_{\mp}(z,t), \tag{2b}$$

$$\tilde{\mathcal{D}}_{\pm}(z,t)=\frac{g'}{\kappa}\mathcal{D}_{\pm}(z,t), \tag{2c}$$

where R is the mirror intensity reflectivity and the field decay rate κ is given by

$$\kappa=\frac{v_0|\ln R|}{2L}\approx\frac{v_0(1-R)}{2L}. \tag{3}$$

In terms of the new dimensionless variables $\tilde{\mathcal{F}}_{\pm}$, $\tilde{\mathcal{B}}_{\mp}$, $\tilde{\mathcal{D}}_{\pm}$, Eqs. (1) take the form

$$\frac{\partial\tilde{\mathcal{F}}_{\pm}}{\partial t}=-\kappa[1-(1-i\alpha)\tilde{\mathcal{D}}_{\pm}]\tilde{\mathcal{F}}_{\pm}-v_0\frac{\partial\tilde{\mathcal{F}}_{\pm}}{\partial z}, \tag{4a}$$

$$\frac{\partial\tilde{\mathcal{B}}_{\mp}}{\partial t}=-\kappa[1-(1-i\alpha)\tilde{\mathcal{D}}_{\pm}]\tilde{\mathcal{B}}_{\mp}+v_0\frac{\partial\tilde{\mathcal{B}}_{\mp}}{\partial z}. \tag{4b}$$

Defining now the z averages

$$F_{\pm}(t)=\frac{1}{L}\int_0^L\tilde{\mathcal{F}}_{\pm}(z,t)dz, \tag{5a}$$

$$B_{\mp}(t)=\frac{1}{L}\int_0^L\tilde{\mathcal{B}}_{\mp}(z,t)dz, \tag{5b}$$

$$D_{\pm}(t)=\frac{1}{L}\int_0^L\tilde{\mathcal{D}}_{\pm}(z,t)dz, \tag{5c}$$

and assuming, thanks to longitudinal quasiuniformity, that the averages of the products are equal to the products of the averages, we obtain from Eqs. (4)

$$\dot{F}_{\pm}=-\kappa[1-(1-i\alpha)D_{\pm}]F_{\pm}-\frac{v_0}{L}[\tilde{\mathcal{F}}_{\pm}^{(2)}-\tilde{\mathcal{F}}_{\pm}^{(1)}], \tag{6a}$$

$$\dot{B}_{\mp}=-\kappa[1-(1-i\alpha)D_{\pm}]B_{\mp}+\frac{v_0}{L}[\tilde{\mathcal{B}}_{\mp}^{(2)}-\tilde{\mathcal{B}}_{\mp}^{(1)}], \tag{6b}$$

where the terms with the superscripts indicate the values of the rescaled fields (2a) and (2b) at the active layer boundaries (1) and (2) (see Fig. 3). Adding Eqs. (6a) and (6b) which govern the averaged counterpropagating fields with opposite helicity and defining

$$E_{\pm}=\frac{F_{\pm}+B_{\mp}}{2}, \tag{7}$$

it turns out that the mean standing fields $E_{\pm}$ of opposite helicity are ruled by the differential equations

$$\dot{E}_{\pm}=-\kappa\left\{[1-(1-i\alpha)D_{\pm}]E_{\pm}+\frac{1}{1-R}[(\tilde{\mathcal{B}}_{\mp}^{(1)}-\tilde{\mathcal{F}}_{\pm}^{(1)})+(\tilde{\mathcal{F}}_{\pm}^{(2)}-\tilde{\mathcal{B}}_{\mp}^{(2)})]\right\}. \tag{8}$$

In the next subsection we will show how the effects of possible small cavity anisotropies can be taken into account in the evaluation of the boundary terms which appear in these equations.

B. Cavity anisotropies

The residual anisotropies of the device are introduced into Eq. (8) by means of the boundary terms: this approach is based on the assumptions that the cavity anisotropies reside mainly in the mirrors and that their effect can be separated from the effect of the active medium. The validity of these assumptions is ensured by the fact that the gain and the anisotropies which act on the propagating fields in a single cavity trip are small.

Taking advantage of the theory developed in [12,13] for phase anisotropies and adapting it to a basis of circularly polarized fields we write

$$\tilde{\mathcal{F}}_{\pm}^{(b)}=M_f\tilde{\mathcal{F}}_{\pm}^{(a)},\quad \tilde{\mathcal{B}}_{\pm}^{(b)}=M_b\tilde{\mathcal{B}}_{\pm}^{(a)}, \tag{9}$$

where the superscripts (a) and (b) indicate two arbitrary transverse sections of the laser resonator, the double subscript sign is now a shorthand notation to indicate 2×1 vectors, and M_f and M_b are 2×2 matrices completely determined by the phase anisotropies which can be present between (a) and (b).

Let us now assume that the (a) and (b) planes coincide respectively with the surface of the lower mirror (see Fig. 3) and the active layer boundary (1). Remembering that the helicity is inverted upon reflection, it is easy to demonstrate the relation

$$\tilde{\mathcal{B}}_{\mp}^{(1)}-\tilde{\mathcal{F}}_{\pm}^{(1)}=[I-M_fT(M_b)^{-1}T]\tilde{\mathcal{B}}_{\mp}^{(1)}, \tag{10}$$

where the symbols I and T denote, respectively, the 2×2 real matrices

$$I=\begin{bmatrix}1&0\\0&1\end{bmatrix},\quad T=\begin{bmatrix}0&1\\1&0\end{bmatrix}. \tag{11}$$

In the same way, by letting the (a) and (b) planes coincide, respectively, with the active layer boundary (2) and the surface of the upper mirror, it can be demonstrated that the second boundary condition is expressed by the relation

$$\tilde{\mathcal{F}}_{\pm}^{(2)}-\tilde{\mathcal{B}}_{\mp}^{(2)}=[I-T(M_b)^{-1}TM_f]\tilde{\mathcal{F}}_{\pm}^{(2)}. \tag{12}$$

We can therefore rewrite the equations (8) that rule the average fields in the form

$$\dot{E}_{\pm}=-\kappa\left\{[1-(1-i\alpha)D_{\pm}]E_{\pm}+\frac{1}{1-R}[M^{(1)}\tilde{\mathcal{B}}_{\mp}^{(1)}+M^{(2)}\tilde{\mathcal{F}}_{\pm}^{(2)}]\right\}, \tag{13}$$

where we have defined

$$M^{(1)}=I-M_f T(M_b)^{-1}T, \tag{14a}$$

$$M^{(2)}=I-T(M_b)^{-1}TM_f, \tag{14b}$$

and used the shorthand notation for the vectors.

Let us now recall that phase anisotropies can be classified as linear or circular, depending on the polarization states between which they introduce a phase difference, and they can be symmetrical or antisymmetrical with respect to time reversal. The general form of the matrix M_f which express the action of phase anisotropies on the forward-propagating field is

$$M_f=\begin{bmatrix} 1-i\delta_c & -i\delta_l \\ -i\delta_l & 1+i\delta_c \end{bmatrix}, \tag{15}$$

where δ_l and δ_c are the (small) phase differences introduced, respectively, between linearly and circularly polarized fields during the propagation from (a) to (b).

The form of the matrix M_b which operates on the backward field depends on the behavior of the anisotropies under time reversal: according to [12], symmetrical and antisymmetrical phase anisotropies are characterized, respectively, by the conditions

$$M_b=(M_f)^*, \tag{16a}$$

$$M_b=[(M_f)^{-1}]^*. \tag{16b}$$

Executing all the operations which appear in the definitions (14) it turns out that in the absence of any anisotropy the matrices $M^{(1)}$ and $M^{(2)}$ are identically equal to the zero matrix, so that all boundary conditions disappear from Eq. (13).

In presence of a linear phase anisotropy we have in the symmetric case

$$M^{(1)}_{l.s.}=M^{(2)}_{l.s.}=\begin{bmatrix} 0 & 2i\delta_l \\ 2i\delta_l & 0 \end{bmatrix}, \tag{17}$$

while in the antisymmetric case all the components of the two matrices are identically equal to zero. We can therefore conclude that the only linear phase anisotropy which can influence the laser dynamics is the symmetric one. Birefringence is an example of such an anisotropy, since a birefringent sample presents two different refractive indices for two orthogonally linearly polarized beams, independently of their propagation direction.

In presence of a circular phase anisotropy we have that in the symmetric case the matrices $M^{(1)}$ and $M^{(2)}$ are identically equal to the zero matrix, while in the antisymmetric case

$$M^{(1)}_{c.a.}=M^{(2)}_{c.a.}=\begin{bmatrix} 2i\delta_c & 0 \\ 0 & -2i\delta_c \end{bmatrix}. \tag{18}$$

We can therefore conclude that the only circular phase anisotropy which can influence the laser dynamics is the antisymmetric one. Optical activity is an example of symmetric circular phase anisotropy: an optically active sample presents two different refractive indices to circularly polarized beams with opposite helicities, independently of their propagation direction. An intuitive explanation of the fact that optical activity does not influence the laser dynamics is that, since circularly polarized light changes the sign of helicity upon reflection, any phase variation built up during the forward trip will be canceled by the backward trip. It is then clear that the only way to provide an effective circular phase anisotropy is to break the system time-reversal symmetry, as can be done, for example, by applying an external magnetic field along the laser cavity. The Faraday effect will cause, in fact, an antisymmetric circular phase anisotropy: the material will again present two different refractive indices to circularly polarized beam with opposite helicities, but the two indices interchange as the beams propagation direction is reversed. As a consequence the phase variation built up during the backward trip will now add with the phase variation built up during the forward trip.

Since we are treating additively the phase anisotropies due to the material birefringence and to the applied magnetic field, we obtain that the matrices $M^{(1)}$ and $M^{(2)}$ which appear in Eqs. (13) are given simply by the sum of the matrices (17) and (18), so that their global action is summarized by the matrix

$$M^{(1)}_{ph}=M^{(2)}_{ph}=\begin{bmatrix} 2i\delta_c & 2i\delta_l \\ 2i\delta_l & -2i\delta_c \end{bmatrix}. \tag{19}$$

To take into account the effects of amplitude anisotropies, the same procedure can be followed. The general form of the matrix M_f which expresses the action of amplitude anisotropies on the forward-propagating field is

$$M_f=\begin{bmatrix} 1-\xi_c & -\xi_l \\ -\xi_l & 1+\xi_c \end{bmatrix}, \tag{20}$$

where ξ_l and ξ_c are the (small) fractional variations in the amplitudes of linearly and circularly polarized fields introduced during the propagation from (a) to (b). Executing the same steps which led us from Eq. (15) to Eq. (19) we conclude again that only symmetric linear and antisymmetric circular amplitude anisotropies can play a role in the laser dynamics, and they are summarized by the matrix

$$M^{(1)}_{am}=M^{(2)}_{am}=\begin{bmatrix} 2\xi_c & 2\xi_l \\ 2\xi_l & -2\xi_c \end{bmatrix}. \tag{21}$$

Treating additively all the anisotropies and making use of the approximation

$$E_{\pm}\approx\frac{\tilde{\mathcal{F}}^{(2)}_{\pm}+\tilde{\mathcal{B}}^{(1)}_{\mp}}{2} \tag{22}$$

which follows from longitudinal quasiuniformity, it is easy to verify that Eqs. (13) can be recasted in the form

$$\dot{E}_{\pm}=-\kappa\{[1-(1-i\alpha)D_{\pm}]E_{\pm}+i(\sigma_l-i\epsilon_l)E_{\mp} \pm i(\sigma_c-i\epsilon_c)E_{\pm}\}, \tag{23}$$

where the linear and circular phase and amplitude anisotropies per field cavity decay time are defined by

$$\sigma_l=\frac{4\delta_l}{1-R}, \quad \epsilon_l=\frac{4\xi_l}{1-R}, \tag{24a}$$

$$\sigma_c=\frac{4\delta_c}{1-R}, \quad \epsilon_c=\frac{4\xi_c}{1-R}. \tag{24b}$$

The signs of these amplitude anisotropies have been chosen in such a way that when $\sigma_l,\sigma_c>0$ and $\epsilon_l,\epsilon_c>0$ the higher-frequency field components have higher losses. As already explained in the introductory remarks, amplitude anisotropies are physically unavoidable in the presence of phase anisotropies and follow from the complex nature of Kramers-Kroning relations: Eq. (23) evidences that they behave as imaginary phase anisotropies. In other terms, we can say that the anisotropies introduce slight modifications in both the real and imaginary parts of the semiconductor complex refractive index n, so that we can write $(n+\delta n)=(n_{re}+\delta n_{re})+i(n_{im}+\delta n_{im})$. Since in a semiconductor the strong inequality $n_{re}\gg n_{im}$ holds (also under lasing conditions), this makes it natural to expect $\delta n_{re}\gg\delta n_{im}$, i.e., that the magnitude of phase anisotropies will be much larger than the magnitude of amplitude anisotropies.

C. Fundamental equations

The global laser dynamics is described by the time evolution of the mean fields $E_\pm$ and of the carrier densities $D_\pm$, which is determined by the nonlinear differential system [10]

$$\dot{E}_\pm=-\kappa[(1-i\alpha)(1-D_\pm)E_\pm+(\epsilon_l+i\sigma_l)E_\mp \pm(\epsilon_c+i\sigma_c)E_\pm], \tag{25a}$$

$$\dot{D}_\pm=-\gamma_\parallel\left[(1+|E_\pm|^2)D_\pm+\frac{\gamma_j}{\gamma_\parallel}(D_\pm-D_\mp)-(1+\beta)\right], \tag{25b}$$

where β is a normalized pumping parameter equal to zero at the lasing threshold and where, with respect to Eq. (23), the reference frequency has been shifted toward the blue by an amount equal to $\kappa\alpha$.

The system of equations (25) lends itself to a global physical interpretation. As shown in Fig. 4, the linear anisotropies provide a direct, coherent coupling between the circularly polarized fields $E_\pm$, while the addition of circular anisotropies causes a variation in the frequencies and in the amplitudes of these fields, thus perturbing their equilibrium states. In absence of any light-material interaction, the interplay between these anisotropies completely determines the VCSEL light polarization. But another field-coupling mechanism comes from the mixing—at the time rate γ_j—between the carrier densities $D_\pm$, and is due to the nonlinear light-material interaction regulated by the pumping strength β and by the linewidth enhancement factor α. This supplementary coupling—which is indirect and incoherent—will modify the polarization of the laser beam, allowing one, in principle, to obtain some insight into the values of the system parameter γ_j.

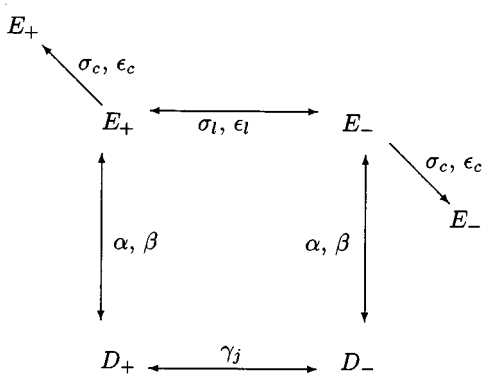

FIG. 4. Physical interplay between the system variables: the linear anisotropies σ_l and ϵ_l provide a direct, coherent coupling between the fields, while the circular anisotropies σ_c and ϵ_c change the amplitude and the frequency of the fields, perturbing their equilibrium positions. The carriers densities are coupled via spin-mixing processes, so that the spin-mixing rate γ_j will also influence the light polarization properties through the nonlinear light-material interaction. This nonlinear interaction is governed by the linewidth enhancement factor α and by the pumping strength β.

To study the polarization properties of VCSEL-generated light it is useful to consider separately the amplitudes and the phases of the fields, writing

$$E_+=|E_+|\exp(-i\phi_+), \tag{26}$$

$$E_-=|E_-|\exp(-i\phi_-), \tag{27}$$

and introduce as new variables the light intensity

$$I=|E_+|^2+|E_-|^2, \tag{28}$$

the ellipticity angle

$$\chi=\arctan\frac{|E_+|-|E_-|}{|E_+|+|E_-|}, \quad -\pi/4\leqslant\chi\leqslant\pi/4, \tag{29}$$

the tilting angle of the major axis of the polarization ellipse

$$\psi=\frac{1}{2}(\phi_+-\phi_-), \quad -\pi/2<\psi\leqslant\pi/2, \tag{30}$$

and the total phase angle

$$\theta=\frac{1}{2}(\phi_++\phi_-), \quad 0\leqslant\theta<2\pi. \tag{31}$$

It is also useful to replace the carrier densities D_+ and D_- with the averaged total carrier density in the material

$$D=\frac{D_++D_-}{2}, \tag{32}$$

and with the averaged difference between the carrier densities available for the two transitions

$$d=\frac{D_+-D_-}{2}. \tag{33}$$

In term of these new variables the system of equations (25) takes the form

$$\dot{I}=2I[D-1-\epsilon_l\cos2\psi\cos2\chi-(\epsilon_c-d)\sin2\chi], \quad (34a)$$

$$\dot{\theta}=\alpha(D-1)+\sigma_l\frac{\cos2\psi}{\cos2\chi}+\epsilon_l\frac{\sin2\psi}{\tan2\chi}, \quad (34b)$$

$$\dot{\chi}=\sigma_l\sin2\psi+\epsilon_l\cos2\psi\sin2\chi-(\epsilon_c-d)\cos2\chi, \quad (34c)$$

$$\dot{\psi}=\sigma_c+\alpha d-(\sigma_l\cos2\psi+\epsilon_l\sin2\psi)\tan2\chi, \quad (34d)$$

$$\dot{d}=-\gamma[d(\Gamma+I)+DI\sin2\chi], \quad (34e)$$

$$\dot{D}=-\gamma[D(1+I)+dI\sin2\chi-(\beta+1)], \quad (34f)$$

where the time has been made dimensionless by means of the inverse field decay time κ (dimensionless time $=\kappa\times$ time). The parameters γ and Γ, which indicate, respectively, the dimensionless inverse carrier radiative lifetime and the normalized spin-mixing rate, are given by

$$\gamma=\frac{\gamma_\parallel}{\kappa}, \quad \Gamma=\frac{\gamma_\parallel+2\gamma_j}{\gamma_\parallel}. \quad (35)$$

The above system of equations constitutes a general tool to analyze the influence of optical anisotropies and of light-material interaction in the polarization properties of the light generated by a VCSEL, and will be the basis of our further investigations.

III. EFFECT OF MATERIAL STRAIN

We start now our analysis of Eqs. (34), concentrating for the moment on the case in which the only anisotropies of the VCSEL are the linear ones, which derive from material strain: in this section we will therefore assume $\sigma_c\equiv\epsilon_c\equiv0$.

It is easy to verify that if also the linear anisotropies σ_l, ϵ_l are equal to zero—that is, if the system is made isotropic—the only possible stationary solution of Eqs. (34) is represented by a linearly polarized field which, due to the rotational invariancy in the transverse plane, is oriented along an arbitrary direction [8]. The introduction of linear anisotropies breaks the transverse rotational invariancy, giving rise—as we will show—to a rich variety of phenomena. In the course of the section we will first concentrate on the role of a phase anisotropy σ_l, and only secondly include in the picture the effects of the amplitude anisotropy ϵ_l which, as discussed at the end of Sec. II B, is unavoidably associated with it but may be expected to be much smaller.

A. Stationary states

When in the system of equations (34) the only anisotropic term different from zero is the linear phase anisotropy σ_l, the stationary values of the light ellipticity angle and of the tilting angle of the ellipse are respectively found to be

$$\tan2\chi=\mp\left[\frac{(\Gamma+I)(\beta-I)}{I-\Gamma(\beta-I)}\right]^{1/2}, \quad (36a)$$

$$\tan2\psi=\pm\left[\frac{(\Gamma+I)(\beta-I)}{\alpha^2I(\beta-I+1)}\right]^{1/2}, \quad (36b)$$

while the active medium is characterized by the carrier densities

$$d=\pm\left[\frac{I(\beta-I+1)(\beta-I)}{(\Gamma+I)}\right]^{1/2}, \quad (37a)$$

$$D=(\beta-I)+1. \quad (37b)$$

In the above relations the light intensity I is a function of the pumping strength β given by either

$$I=\beta \quad (38)$$

or

$$I=I_{\alpha,\Gamma,\sigma_l}(\beta). \quad (39)$$

These two possibilities are, respectively, responsible for the creation of linearly and elliptically polarized states. The function $I_{\alpha,\Gamma,\sigma_l}(\beta)$ is obtained from the equation

$$\mathcal{P}(I)=\left[(\beta-I)+\frac{(\alpha d)^2}{(\beta-I)}\right][\Gamma(\beta-I)-I]+\sigma_l^2(\Gamma+I), \quad (40)$$

under the restriction

$$\beta\frac{\Gamma}{1+\Gamma}<I\leqslant\beta, \quad (41)$$

which is dictated by the constraint that the expressions (36) of the angles χ and ψ are real valued: using Eq. (37b), it is easy to demonstrate that these two inequalities can be rewritten in the form

$$0\leqslant D-1<\frac{\beta}{1+\Gamma}. \quad (42)$$

It must be stressed that when the only nonzero anisotropic term present in Eqs. (34) is the linear phase anisotropy σ_l, the system is invariant under the transformation

$$\begin{aligned}&\chi\rightarrow-\chi,\\&\psi\rightarrow-\psi,\\&d\rightarrow-d,\end{aligned} \quad (43)$$

so that any elliptically polarized solution $(\tilde{\chi},\tilde{\psi})$ will always give rise to two coexisting states,

$$(\chi,\psi)=\begin{cases}\tilde{\chi},\tilde{\psi},\\-\tilde{\chi},-\tilde{\psi}.\end{cases} \quad (44)$$

The stationary values of the system variables given by Eqs. (36) and (37) have been represented as functions of the pumping strength β in Fig. 5, with the system parameters fixed to the values $\alpha=4$, $\Gamma=100$, and $\sigma_l=0.035$. In Fig. 5(a) is shown the ellipticity $\tan2\chi$: the straight line represents the linearly polarized state characterized by the intensity $I=\beta$, while the bifurcating branches represent the ellip-

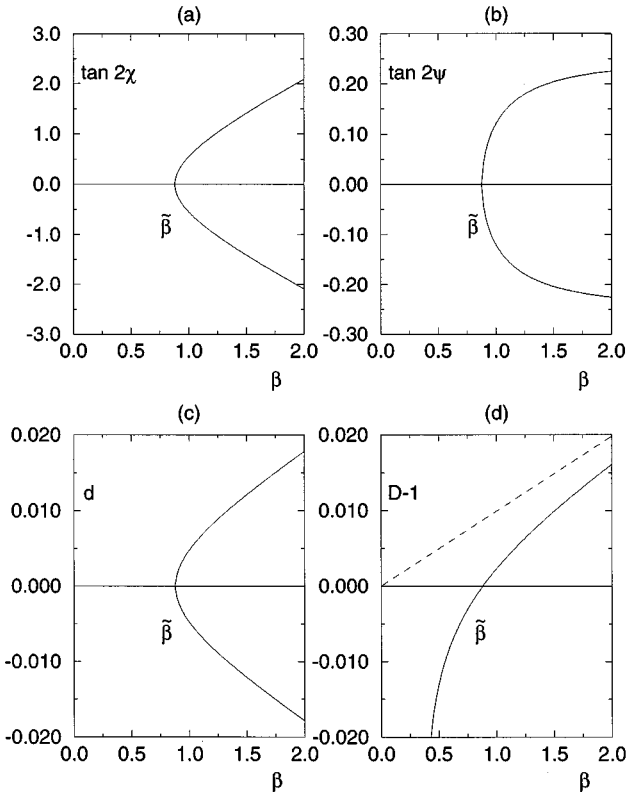

FIG. 5. Representation of the system stationary states determined by Eqs. (36) and (37). The values of the system parameters are, respectively, $\alpha=4$, $\Gamma=100$, and $\sigma_l=0.035$. See the text for explanations.

tically polarized states characterized by the intensity $I=I_{\alpha,\Gamma,\sigma_l}(\beta)$ and opposite signs of 2χ. The tilting $\tan 2\psi$ is shown in Fig. 5(b): the straight line represents the linearly polarized state of intensity $I=\beta$, while the bifurcating branches represent the elliptically polarized states of intensity $I=I_{\alpha,\Gamma,\sigma_l}(\beta)$ and opposite signs of 2ψ. Note that the scale of the ordinate axis is 1/10 as compared with Fig. 5(a). In Fig. 5(c) we have represented the carrier difference d: the straight line and the bifurcating branches represent, respectively, the linearly polarized state and the two coexisting elliptically polarized states. Finally, in Fig. 5(d) the continuous line represents the carrier density $D-1$, and the dashed one indicates the function $\beta/(1+\Gamma)$: it is clear that the first of the conditions expressed by Eq. (42) imposes on the pumping parameter the inequality $\beta\geqslant\tilde{\beta}$ in order to obtain elliptically polarized states; the other condition, on the contrary, is always satisfied. The value $\tilde{\beta}$ sets a bifurcation point for the system, because for $\beta\geqslant\tilde{\beta}$ two states with opposite values of the angles χ and ψ and of the carrier difference d will be possible. To calculate $\tilde{\beta}$ we solve the equation

$$\mathcal{P}(\tilde{\beta})=0, \tag{45}$$

which follows from Eq. (40), obtaining

$$\tilde{\beta}=\frac{\Gamma\sigma_l}{\alpha-\sigma_l}. \tag{46}$$

From the stationary solutions of Eqs. (34c) and (34d), it can be easily verified that the ellipticity and the tilting angles satisfy the relation

$$\sin 2\chi+\alpha\tan 2\psi=0, \tag{47}$$

so that ellipticity is naturally associated with tilting.

It is also evident from Fig. 5 that close to threshold the only possible states of the fields are linearly polarized: from Eq. (34b) we deduce that their frequencies are, respectively, $\dot{\theta}=+\sigma_l$ for $\psi=0$ and $\dot{\theta}=-\sigma_l$ for $\psi=\pi/2$. Accordingly, they will be indicated respectively by high and low. In the next subsection we will investigate their stability properties.

B. Stability of the stationary states

A linear stability analysis of the two linearly polarized solutions

$$I=\beta,\quad \dot{\theta}=+\sigma_l,\quad \chi=0,\quad \psi=0,\quad D=1,\quad d=0,\qquad \text{high (hi)} \tag{48}$$

$$I=\beta,\quad \dot{\theta}=-\sigma_l,\quad \chi=0,\quad \psi=\pi/2,\quad D=1,\quad d=0,\qquad \text{low (lo)}$$

reveals, in accordance with [10], that the high-frequency one is stable when

$$\beta>\frac{2\alpha\sigma_l}{\gamma}-\Gamma, \tag{49}$$

and the low-frequency one when

$$\beta<\frac{\Gamma\sigma_l}{\alpha-\sigma_l}. \tag{50}$$

We can therefore divide the (σ_l,β) plane into the four regions shown in Fig. 6(a) and labeled with ''hi'' and/or ''lo'' to indicate the system stationary stable states. Since a numerical analysis reveals that in the domain indicated by the shadowed band also elliptically polarized states are stable, we deal with the following situations:

(i) hi domain: only the high linearly polarized state is stable;

(ii) lo domain: only the low linearly polarized state is stable;

(iii) hi-lo domain: coexistence of the two linearly polarized states;

(iv) el domain: coexistence of two elliptically polarized states, which destabilize the lo state;

(v) hi-el domain: coexistence among the high linearly polarized state and the two elliptically polarized ones;

(vi) dy domain: the light polarization changes dynamically in time, and does not reach any stationary stable state.

For completeness we now analyze how the situation described above is modified by the action of a linear amplitude anisotropy ϵ_l, which takes into account polarization-dependent losses or gain. If we assume that in the system of equations (34) the anisotropic terms different from zero are σ_l and ϵ_l, we find that states with linear polarization are still possible and given by

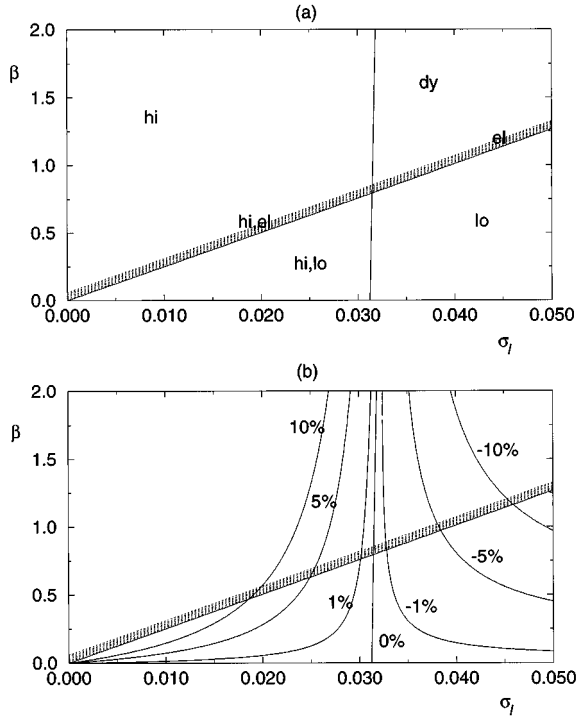

FIG. 6. (a) Domains of different behaviors for light polarization in the presence of a linear phase anisotropy σ_l only, with $\alpha=4$, $\Gamma=100$, and $\gamma=0.0025$. In the hi and lo domains only one of the two possible linearly polarized states is possible, while in the hi-lo domain there is bistability among them. The el label and the shadowing indicate the narrow stability domain for elliptically polarized states, and the dy label indicates the region in which the polarization characteristics of the laser beam change dynamically in time. (b) Domains of different behaviors for light polarization in the presence of linear phase and amplitude anisotropies σ_l and ϵ_l, with $\alpha=4$, $\Gamma=100$, and $\gamma=0.0025$. The linear amplitude anisotropy ϵ_l has a modulus equal to 0%, 1%, 5%, and 10% of the modulus of the linear phase anisotropy σ_l; both the cases of positive and negative sign are considered, and represented by the sign in front of the percentage. Note that positive (negative) values of ϵ_l reduce (increase) the extension of the stability domain of the high-frequency state, which has higher (lower) losses with respect to the low-frequency one. The boundaries of the stability domain of the low-frequency state depend much less on ϵ_l, and their variation cannot be seen in the figure.

$$I=\frac{\beta-\epsilon_l}{1+\epsilon_l},\quad \dot{\theta}=+(\sigma_l+\alpha\epsilon_l),\quad \chi=0,\quad \psi=0,$$

$$D=1+\epsilon_l,\quad d=0,\ \text{high (hi)} \tag{51}$$

$$I=\frac{\beta+\epsilon_l}{1-\epsilon_l},\quad \dot{\theta}=-(\sigma_l+\alpha\epsilon_l),\quad \chi=0,\quad \psi=\pi/2,$$

$$D=1-\epsilon_l,\quad d=0,\ \text{low (lo)}.$$

A linear stability analysis reveals that the condition (49) for the stability of the high-frequency state is generalized by the inequality

$$A\beta^2+B\beta+C>0, \tag{52}$$

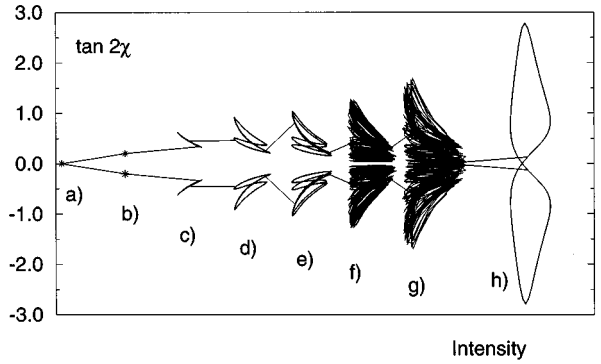

FIG. 7. Ellipticity $\tan 2\chi$ versus intensity I for increasing values of the pumping β: a: $\beta=0.8$; b: $\beta=0.9$; c: $\beta=1.0$; d: $\beta=1.05$; e: $\beta=1.07$; f: $\beta=1.1$; g: $\beta=1.15$; h: $\beta=1.90$. The values of the other parameters are $\alpha=4$, $\Gamma=100$, $\gamma=0.0025$, and $\sigma_l=0.035$.

with the coefficients A, B, C respectively given by

$$A=\gamma, \tag{53a}$$

$$B=(1+\epsilon_l)^2(\gamma\Gamma-2\epsilon_l-2\alpha\sigma_l)+2\epsilon_l(1+\epsilon_l)(\epsilon_l-\gamma\Gamma)+2\gamma\epsilon_l^2, \tag{53b}$$

$$C=[(1+\epsilon_l)^2(\gamma\Gamma-2\epsilon_l-2\alpha\sigma_l)-2\epsilon_l(1+\epsilon_l)(\epsilon_l-\gamma\Gamma)-2\gamma\epsilon_l^2+(1+\epsilon_l)^2(2\epsilon_l\Gamma-\gamma\Gamma)]\epsilon_l. \tag{53c}$$

On the other hand, the condition (50) for the stability of the low-frequency states becomes

$$\beta<\frac{(1-\epsilon_l)(\sigma_l\Gamma+\epsilon_l\alpha)+\sigma_l\epsilon_l}{\alpha(1-\epsilon_l)-\sigma_l}. \tag{54}$$

Figure 6(b) shows the influence of the linear amplitude anisotropy on the system stability domains; to plot it we have fixed the magnitude of the amplitude anisotropy at 1–10 % of the phase anisotropy. This range is based on the observed widths of the peaks associated with the two polarization modes in the VCSEL emission spectra below threshold [11]. Note that the variation of Eq. (54) with respect to Eq. (50) is so small that it is not visible in Fig. 6(b), while the variation of Eq. (52) with respect to Eq. (49) is substantial. It can be observed that the sign of ϵ_l determines the system stable states when the laser is close to threshold, but the influence of the amplitude anisotropy diminishes as the pumping parameter β is increased. Switching among the high- and low-frequency states upon raising and lowering the value of the pumping parameter β has been numerically demonstrated in [10].

Having determined the light polarization stationary states, we give now a description of the behavior of the laser in the dy domain, where the polarization characteristics change dynamically in time. Therefore we choose the linear phase anisotropy σ_l large enough so that increasing the value of the pumping parameter β lifts the system from the stationary lo and el domains up to the dy one [see Fig. 6(a)]. In Fig. 7 the light ellipticity has been plotted as a function of the intensity for the various values of the pumping. Inside the lo domain the laser state is represented by a point at zero ellipticity

(a), but when the pumping is increased and the laser is brought inside the el domain two states of opposite ellipticity are stable (b). If the pumping is further increased each point becomes a closed ring (c), indicating that now the system stable states are no longer stationary but periodically oscillating. The ring is then transformed in an eight (d), indicating a doubling of the oscillating period: the eight duplicates (e) and duplicates again, up to the situation represented in f: note that the system still exhibits the coexistence of two (nonstationary) states in such a way that the average value of the ellipticity for each of them is different from zero. Only when the interaction between the two coexisting states gives rise to the situation shown in g does the time-averaged value of the ellipticity become zero. For higher values of the pumping the system reaches again a quasiperiodic stable state, as shown in h, and here again the average light ellipticity will be equal to zero.

We end the present section remarking the large influence of the value of the normalized spin-mixing rate Γ on the boundaries of the domains shown in Fig. 6, and therefore on the general polarization behavior of the laser beam. For a comparison with the experimental findings, a reliable determination of Γ is therefore a task of primary importance. This is the topic of the next section.

IV. EFFECTS OF MAGNETIC FIELD

In this section we study how an external magnetic field longitudinally applied along the VCSEL affects the polarization characteristics of the laser beam and thus forms a tool to measure Γ. Since the main consequence of such a field is the creation of a circular phase anisotropy σ_c in the system of Eqs. (34), we are now extending its analysis to the case in which both linear and circular phase anisotropies are different from zero.

A major consequence of the presence of σ_c is the breaking of the system invariance under the transformation given by Eq. (43): as a result, we can no longer expect any linearly polarized states or coexistence of states with opposite ellipticity. We will see in fact that the laser beam will be always elliptically polarized, and that the sign of the ellipticity angle is fully determined by the sign of the anisotropies.

In order to allow a comparison with the experimental situation described in [11], we concentrate on circular phase anisotropies much smaller than the linear phase anisotropy, and we fix this latter at a value large enough to avoid the bistability domain shown in Fig. 6, since bistable behavior close to threshold is never met in our experiment [11]. With these choices, the laser exhibits a prevalence of stationary stable states.

A. Stationary states

When in Eqs. (34) the only anisotropic terms different from zero are the linear and circular phase anisotropies σ_l and σ_c, the stationary values of the light ellipticity angle and of the tilting angle of the ellipse are, respectively, found to be

$$\tan 2\chi = \mp\left[\frac{(\Gamma+I^{\pm})(\beta-I^{\pm})}{I^{\pm}-\Gamma(\beta-I^{\pm})}\right]^{1/2}, \tag{55a}$$

$$\tan 2\psi = \frac{\beta-I^{\pm}}{\sigma_c \pm \alpha[I^{\pm}(\beta-I^{\pm})(\beta-I^{\pm}+1)/(\Gamma+I^{\pm})]^{1/2}}, \tag{55b}$$

while the active medium is characterized by the carrier densities

$$d = \pm\left[\frac{I^{\pm}(\beta-I^{\pm}+1)(\beta-I^{\pm})}{(\Gamma+I^{\pm})}\right]^{1/2}, \tag{56a}$$

$$D = (\beta-I^{\pm})+1. \tag{56b}$$

Note that since the system given by Eqs. (34a) is no longer invariant under the transformation represented by Eq. (43), the light intensity in the above relations is not the same for the upper and lower signs. In fact, it is given in the two cases, respectively, by

$$I = I^{+}_{\alpha,\Gamma,\sigma_l,\sigma_c}(\beta) \tag{57}$$

and

$$I = I^{-}_{\alpha,\Gamma,\sigma_l,\sigma_c}(\beta). \tag{58}$$

The two functions $I^{\pm}_{\alpha,\Gamma,\sigma_l,\sigma_c}$ are obtained from the equation

$$\mathcal{Q}(I) = \left[(\beta-I)+\frac{(\sigma_c+\alpha d)^2}{(\beta-I)}\right][\Gamma(\beta-I)-I]+\sigma_l^2(\Gamma+I). \tag{59}$$

Using Eqs. (34c) and (34d) it is easy to verify that in stationary conditions the ellipticity and the tilting angle satisfy the relation

$$\sin 2\chi + \alpha \tan 2\psi = \frac{\sigma_c}{\sigma_l}\frac{\cos 2\chi}{\cos 2\psi} \tag{60}$$

which generalizes Eq. (47).

The stationary values of the system variables given by Eqs. (55) and (56) are shown in Fig. 8 as functions of the pumping strength β for the different values of circular phase anisotropy $\sigma_c = 0.000$, 0.002, 0.004, 0.006, 0.008, and 0.010 and for the same values of the system parameters used in Fig. 5. In Fig. 8(a) is shown the ellipticity $\tan 2\chi$: the dotted and the solid lines represent, respectively, the states I^{-} and I^{+}, which for $\sigma_c \to 0$ collapse, respectively, towards the linearly polarized solutions and the lower of the bifurcating branches of Fig. 5(a), which is represented by the dashed line. The tilting $\tan 2\psi$, the carrier density difference d, and the carrier density $D-1$ are shown with the same conventions in Figs. 8(b)–8(d): by comparison with Figs. 5(b)–5(d) it can be noted that the tilting and the carrier density difference approach, among the two available branches, the higher one.

For clarity we have represented in Fig. 8 only the effect of a positive circular phase anisotropy σ_c, and among the two bifurcating branches depicted in Fig. 5 we have drawn only that one which the system approaches as $\sigma_c \to 0$. But it is easy to verify from Eq. (59) that, if the sign of σ_c is reversed, the system (34) remains unchanged upon reversing the signs of d, χ, and ψ: as a consequence, the laser will approach the second of the bifurcating branches.

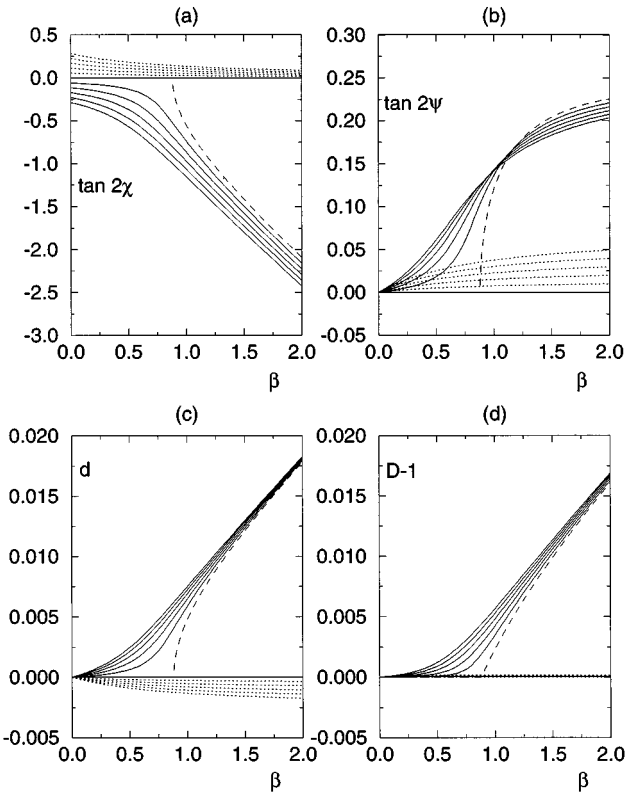

FIG. 8. Representation of the system stationary states determined by Eqs. (55) and (56). The values of the system parameters are, respectively, $\alpha=4$, $\Gamma=100$, and $\sigma_l=0.035$, while the circular phase anisotropy assumes the increasing values $\sigma_c=0.000$, 0.002, 0.004, 0.006, 0.008, and 0.010. See the text for explanations.

A numerical analysis of the stability properties of the stationary states shows that the only solutions which are stable close to threshold are those characterized by the intensity I^+, which have been represented by means of the solid lines; if the pumping parameter β is increased above a certain value these states also will become unstable, as we will show later.

We conclude that in the presence of a circular phase anisotropy σ_c (i) all stationary states become elliptically polarized, (ii) the states which are stable near threshold arise from the bifurcating solutions we met in Sec. III, and (iii) the coexistence between two states with opposite ellipticity is removed in such a way that the system is forced into one of them. In addition, the stationary values of the system variables change: comparing in Fig. 8 the solid lines with the dashed bifurcating branches, we can see that this change is maximum in the neighborhood of the system bifurcation point and becomes smaller in percentage as the pumping parameter is increased.

In Figs. 9(a)–9(b) we have represented the ellipticity and the frequency of the stable states as functions of the circular phase anisotropy for different values of the material birefringence. Note that the ellipticity has initially a linear dependence and saturates only for higher values of the circular anisotropy, while the laser frequency is, for small values of σ_c, a parabolic function of the circular phase anisotropy.

To describe the destabilization process of these states, we have plotted in Fig. 10 their ellipticity tan2χ as a function of

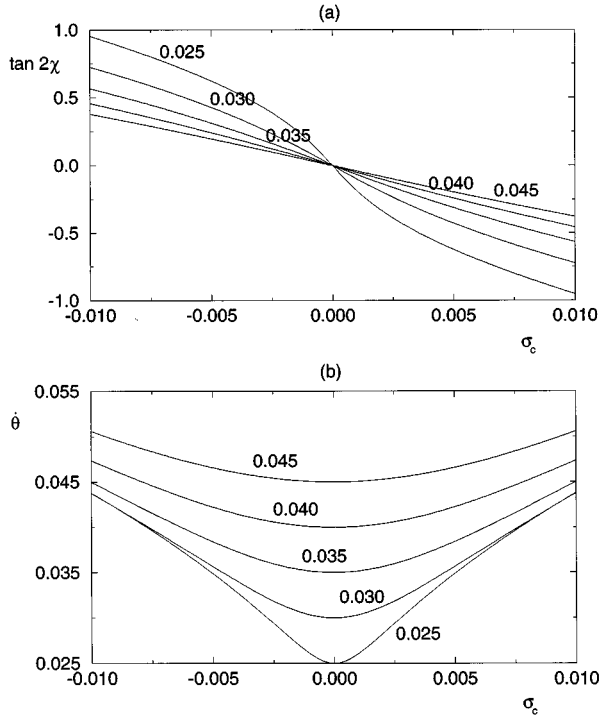

FIG. 9. Ellipticity tan2χ (a) and frequency $\dot{\theta}$ (b) versus circular phase anisotropy σ_c for increasing values of linear phase anisotropy $\sigma_l=0.025$, 0.030, 0.035, 0.040, and 0.045; the values of the fixed parameters are $\alpha=4$, $\Gamma=100$, and $\beta=0.5$. Note that under the condition $\sigma_c \ll \sigma_l$ the ellipticity and the frequency are, respectively, linear and parabolic functions of the circular phase anisotropy.

the light intensity I for various values of the pumping strength β. Since we have $I \approx \beta$ the ellipticity lines drawn in Fig. 10 as functions of the intensity can be identified with those shown in Fig. 8(a) as functions of the pumping strength. The continuous lines mark the states which are numerically found to be stable, while the dotted ones indicate the unstable states: it can be noted that all the stationary solutions are stable close to threshold, and that the lower the magnitude of σ_c, the wider is their stability domain. The

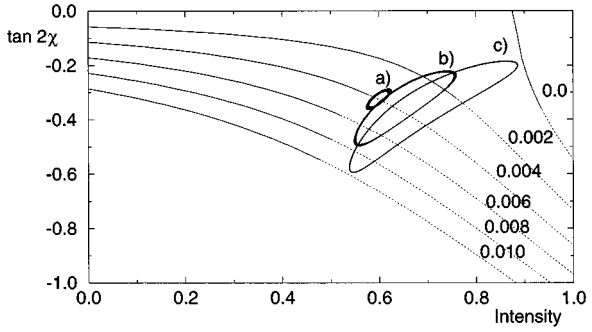

FIG. 10. Ellipticity tan2χ versus intensity I for different values of circular phase anisotropy: $\sigma_c=0.000$, 0.002, 0.004, 0.006, 0.008, and 0.010. Continuous and dotted lines indicate, respectively, stable and unstable stationary states. In unstable states the intensity and ellipticity oscillate periodically around their stationary values, as indicated by the three circles for $\sigma_c=0.004$ and $\beta=0.60$, 0.65, and 0.70. The values of the other parameters are $\alpha=4$, $\Gamma=100$, $\gamma=0.0025$, and $\sigma_l=0.035$.

destabilization has the form of periodic oscillations around the predicted stationary values of the variables, as indicated by the rings. We have observed that if we add a positive circular amplitude anisotropy ϵ_c in the dynamical equations (34) the amplitude of the oscillations is reduced, or—in other terms—the rings collapse. As a consequence, the stability domains extend toward higher values of β, while the ellipticity does not shift appreciably from the stationary values calculated in the absence of ϵ_c.

B. Analytical solutions close to threshold

Explicit expressions for the stationary values of the system variables as functions of the various parameters can be obtained if they are expanded as geometrical series in the pumping strength β and if it is assumed that the laser is so close to threshold that only terms up to the first order need to be included. In this way we can obtain a linear approximation of the influence of the nonlinear light-material interaction on the polarization properties of the laser light. For the stable states considered up to now we have, under the further assumption $\sigma_c \ll \sigma_l$,

$$I = \left(1 - \frac{\sigma_c^2}{\Gamma \sigma_l^2}\right)\beta, \tag{61a}$$

$$\dot{\theta} = \sigma_l + \frac{\sigma_c^2}{2\sigma_l}\left(1 + \frac{4\alpha\beta}{\Gamma\sigma_l}\right), \tag{61b}$$

$$\tan 2\chi = -\frac{\sigma_c}{\sigma_l}\left(1 + \frac{\alpha\beta}{\Gamma\sigma_l}\right), \tag{61c}$$

$$\tan 2\psi = \frac{\sigma_c \beta}{\Gamma \sigma_l^2}, \tag{61d}$$

$$d = \frac{\sigma_c \beta}{\Gamma \sigma_l}, \tag{61e}$$

$$D = 1 + \frac{\sigma_c^2 \beta}{\Gamma \sigma_l^2}. \tag{61f}$$

Using Eq. (61e), the expression obtained for the ellipticity angle can be recast in the form

$$\tan 2\chi = -\frac{\sigma_c + \alpha d}{\sigma_l}, \tag{62}$$

which shows that, in first order, the effect of the material is to increase the circular phase anisotropy by an amount equal to αd. The origin of this phenomenon can be tracked back to the set of Eqs. (34), and in particular to Eqs. (34a), (34c), and (34d): we can say that a carrier density difference d modifies the circular amplitude and phase anisotropies ϵ_l and σ_l in such a way that their effective values will be given, respectively, by

$$\epsilon_c^{\text{eff}} = \epsilon_c - d, \tag{63a}$$

$$\sigma_c^{\text{eff}} = \sigma_c + \alpha d. \tag{63b}$$

We can see from Fig. 8(c) that, as the pumping is increased, a difference d arises between the carrier densities available for the two circular eigenmodes: this difference causes a variation in the circular amplitude anisotropy ϵ_c and, due to the dependence of the refractive index on the carrier density mediated by the α factor, also in the circular phase anisotropy σ_c. The effective value of σ_c is therefore determined by Eq. (63b), and as a result the light ellipticity will be given by Eq. (62). The smaller the value of Γ, the less efficient are the spin-mixing processes, and consequently the larger the carrier difference d, leading to an enhancement of the nonlinear contributions to the anisotropies. We can therefore understand why the pumping parameter β always appears in Eqs. (61) divided by Γ, and in Eq. (61c) multiplied by α.

We also note that this linearized approach to take into account the nonlinear light-material interaction is bound to fail as the pumping strength approaches the value $\tilde{\beta}$, since a bifurcation constitutes a phenomenon which cannot be explained on the basis of a linear model. As a consequence, the approximate linearized solutions (61) are valid under the condition

$$\beta \ll \tilde{\beta} = \frac{\Gamma \sigma_l}{\alpha - \sigma_l} \tag{64}$$

which becomes more stringent as α is increased and Γ decreased, that is, when the action of nonlinear effects is more appreciable.

As a final note, we stress that Eqs. (61b) and (61c) for the light frequency and ellipticity near threshold deserve particular attention, given the experimental measurability of these variables. It has been, in fact, by fitting them to experimental data [11] that we have obtained the value $\Gamma \approx 100$ used in the numerical simulations (see discussion of parameter values in Sec. V).

V. CONCLUSIONS

Let us now summarize the effects of linear and circular phase anisotropies on the polarization characteristics of VCSEL's light. We already knew [8] that in the absence of any anisotropy the light is linearly polarized and the field is oriented along an arbitrary direction of the transverse plane. When a linear phase anisotropy is added, the transverse rotational invariancy is broken, and in accordance with [10], the following results have been demonstrated.

(1a) Linearly polarized solutions are still possible, but now the field can be oriented only along the two orthogonal directions of the transverse plane characterized, respectively, by the minimum and maximum values of the refractive index [see the lines $\tan 2\chi = 0$ and $\tan 2\psi = 0$ in Figs. 5(a) and 5(b)]. The continuum of states available in the isotropic case is then drastically reduced, and depending on the system parameters the laser chooses one of the two states now available, or may even be bistable [see Fig. 6(a)]. The extension of the bistability domain is demonstrated to depend critically on the possible presence of linear amplitude anisotropies [see Fig. 6(b)].

(1b) The coherent coupling between fields with opposite circular polarization allows the creation of states that, when the pumping parameter exceeds a certain value, acquire an

ellipticity. Due to the system invariance under the transformation (43), states of opposite ellipticity are always coexisting [see the bifurcating curve in Figs. 5(a) and 5(b)]. The domain of the parameter space in which elliptically polarized states are stationary is rather small: the system usually orbits around one of them or it may even oscillate between states with opposite ellipticity, thus exhibiting a time-averaged ellipticity equal to zero (see Figs. 6 and 7).

As compared with this situation, the further presence of a circular phase anisotropy produced by a magnetic field has as a main consequence the breaking of the system invariancy under the transformation (43), thus forbidding both the possibility (1a) of linearly polarized states and the possibility (1b) of coexisting states with opposite ellipticity. We have demonstrated, in fact, the following.

(2a) The states which were linearly polarized become elliptically polarized, and their ellipticity decreases with pumping [see the dashed lines in Figs. 8(a) and 8(b)]; these states are found to be always unstable near the lasing threshold.

(2b) The states which were elliptically polarized only for large enough values of the pumping parameter are now always elliptically polarized, and the sign of the ellipticity is determined by the signs of the linear and circular phase anisotropies. The ellipticity increases with pumping [see the continuous lines in Figs. 8(a) and 8(b)], and these states are found to be stationary up to a certain value of the pumping parameter (see Fig. 10).

We can therefore say that the lasing fields generated by the two electronic transitions $m_j = \pm 1/2 \rightarrow \pm 3/2$ depending on the values of the system parameters, (i) can realize a spontaneous phase and frequency locking, giving rise to stationary linear or elliptical polarization, respectively, if they oscillate with the same or different amplitudes or (ii) do not realize a spontaneous phase and frequency locking, giving rise to a time-dependent polarization, characterized by periodic oscillations, period doubling, and possibly chaos.

As a further conclusion, we stress that the polarization properties of VCSEL's are determined both by the linear couplings between the circularly polarized fields provided by the residual cavity anisotropies and by the nonlinear couplings among the fields and the carrier densities. The smaller the linear couplings, the more prominent the role of the nonlinear ones: in particular, if the linear anisotropies of the VCSEL are set equal to zero (this experiment is in progress in our laboratory), we should recover the same behavior of gas lasers under a small magnetic field, that is, a rotating linear polarization. In this case the two circularly polarized fields oscillate with the same amplitude, but—since there is no longer a direct and coherent coupling between them—they do not lock their frequencies.

We remark that all the values of the parameters used for the figures are realistic from the experimental point of view: in Fig. 6, for example, with $\kappa = 3 \times 10^{11}\ \mathrm{s}^{-1}$, the frequency separation between linearly polarized fields $\Delta\nu = 2\sigma_l\kappa/(2\pi)$ ranges up to 5 GHz for $\sigma_l = 0.05$, which is a typical value observed in VCSEL's. The value of Γ has been obtained by fitting the theoretical relation Eqs. (61b) and (61c) to experimental data [11], obtaining $\Gamma \approx 100$; assuming $\gamma_\parallel = 0.75 \times 10^9\ \mathrm{s}^{-1}$, we obtain from the second of Eqs. (35) the value $\gamma_j = 3.7 \times 10^{10}\ \mathrm{s}^{-1}$, which is in the middle of the range mentioned in Refs. [17,18]. The value $\alpha = 4$ for the linewidth enhancement factor is commonly accepted in the literature on semiconductor lasers and has been recently measured also in VCSEL's [20].

Finally, we hope that our theoretical investigation will stimulate further experimental work on VCSEL's polarization behavior, and in particular on magnetically induced ellipticity. In addition, it will be interesting to see if other regions of the parameter space than those stressed in the present paper are also experimentally accessible.

Note added: Recently we became aware that for the case of a linear amplitude anisotropy similar results were obtained by J. Martin-Regalado, F. Prati, M. San Miguel, and N. B. Abraham (unpublished). Also, we received a copy of unpublished work by C. Serrat, N.B. Abraham, M. San Miguel, R. Vilaseca, and J. Martin-Regalado giving a description of the dynamical polarization behavior of the VCSEL under the action of a very strong axial magnetic field.

ACKNOWLEDGMENTS

We are glad to acknowledge useful discussions with M. San Miguel and F. Prati. The research of M. Travagnin was supported by the Human Capital and Mobility program of the European Community under the Contracts No. ERBCHBGCT 930437 and No. CHRX-CT93-0114, by the ESPRIT project 20029 ACQUIRE and by the TMR network ERB4061PL951021. The work of M.P. van Exter was supported by the Royal Dutch Academy of Arts and Sciences. This work is part of the research program of the ''Stichting voor Fundamenteel Onderzoek der Materie (FOM).''

[1] K. Iga, F. Koyama, and S. Kinoshita, IEEE J. Quantum Electron. **24**, 1845 (1988).
[2] J. L. Jewell, J. P. Harbison, A. Schrerer, Y. H. Lee, and L. T. Florentz, IEEE J. Quantum Electron. **27**, 1332 (1991).
[3] J. L. Jewell, S. L. McCall, Y. H. Lee, A. Scherer, A. C. Gossard, and J. H. English, Appl. Phys. Lett. **54**, 1400 (1989).
[4] C. J. Chang-Hasnain, J. P. Harbison, L. T. Florez, and N. G. Stoffel, Electron. Lett. **27**, 163 (1991).
[5] C. J. Chang–Hasnain, J. P. Harbison, G. Hasnain A. C. Von Lehmen, L. T. Flores, and N. G. Stoffel, IEEE J. Quantum Electron. **27**, 1402 (1991).
[6] Z. George Pan, Shijun Jiang, Mario Dagenais, Robert A. Morgan, Keisuke Kojima, Moses T. Asom, Ronald E. Leibenguth, Gregory D. Guth, and Marlin W. Focht, Appl. Phys. Lett. **63**, 2999 (1993).
[7] Kent D. Choquette, D. A. Richie, and R. E. Leibenguth, Appl. Phys. Lett. **64**, 2062 (1994).
[8] M. San Miguel, Q. Feng, and J. V. Moloney, Phys. Rev. A **52**, 1728 (1995).
[9] C. H. Henry, IEEE J. Quantum Electron. **18**, 259 (1982).
[10] J. Martin-Regalado, M. San Miguel, N. B. Abraham, and F. Prati, Opt. Lett. **21**, 351 (1995).

[11] A. K. Jansen van Doorn, M. P. van Exter, M. Travagnin, and J. P. Woerdman (unpublished).
[12] D. Lenstra and S. H. M. Geurten, Opt. Commun. **75**, 63 (1990).
[13] R. J. C. Spreeuw, M. W. Beijersbergen, and J. P. Woerdman, Phys. Rev. A **45**, 1213 (1992).
[14] W. W. Chow, S. W. Koch, and M. S. Sargeant III, *Semiconductor Lasers Physics* (Springer-Verlag, Berlin, 1994).
[15] P. S. Zory, *Quantum Well Lasers* (Academic, San Diego, 1993).
[16] L. Mandel and E. Wolf, *Optical Coherence and Quantum Optics* (Cambridge University Press, Cambridge, England, 1995).
[17] R. Ferreira and G. Bastard, Phys. Rev. B **43**, 9687 (1991).
[18] M. Z. Maialle, E. A. de Andrada e Silva, and L. J. Sham, Phys. Rev. B **47**, 15 776 (1993).
[19] F. Prati, A. Tesei, L. Lugiato, and R. J. Horowicz, Chaos, Solitons Fractals **4**, 1637 (1994).
[20] D. Kuksenkov, S. Feld, C. Wilmsen, H. Temkin, S. Swirhun, and R. Leibenguth, Appl. Phys. Lett. **66**, 277 (1995).